

# GeodesicNVS: Probability Density Geodesic Flow Matching for Novel View Synthesis

Xuqin Wang<sup>1,2</sup> Tao Wu<sup>1</sup> Yanfeng Zhang<sup>1</sup> Lu Liu<sup>1</sup> Mingwei Sun<sup>1</sup> Yongliang Wang<sup>1</sup>  
 Niclas Zeller<sup>2,3</sup> Daniel Cremers<sup>2</sup>  
<sup>1</sup>Huawei Dresden Research Center  
<sup>2</sup>Technical University of Munich  
<sup>3</sup>Karlsruhe University of Applied Sciences

## Abstract

*Recent advances in generative modeling have substantially enhanced novel view synthesis, yet maintaining consistency across viewpoints remains challenging. Diffusion-based models rely on stochastic noise-to-data transitions, which obscure deterministic structures and yield inconsistent view predictions. We propose a Data-to-Data Flow Matching framework that learns deterministic transformations directly between paired views, enhancing view-consistent synthesis through explicit data coupling. To further enhance geometric coherence, we introduce Probability Density Geodesic Flow Matching (PDG-FM), which constrains flow trajectories using geodesic interpolants derived from probability density metrics of pretrained diffusion models. Such alignment with high-density regions of the data manifold promotes more realistic interpolants between samples. Empirically, our method surpasses diffusion-based NVS baselines, demonstrating improved structural coherence and smoother transitions across views. These results highlight the advantages of incorporating data-dependent geometric regularization into deterministic flow matching for consistent novel view generation.*

## 1. Introduction

Novel View Synthesis (NVS) aims to generate unseen views of a scene from a limited set of observations. Despite the rapid progress of generative models, achieving consistent and geometry-aware view generation remains challenging. Recent advances in diffusion-based models have shown strong performance in generating high-quality single-view or multi-view images, yet these models often struggle to maintain structural coherence across different viewpoints. However, achieving consistent viewpoint synthesis remains challenging, as most generative models lack explicit modeling of the underlying geometric relationships between

views [25, 33].

Flow Matching (FM) [1, 18, 21] provides a deterministic alternative, learning continuous-time dynamics between data distributions. Conditional Flow Matching (CFM) [1, 18, 21] extends this concept to conditional distributions, enabling mappings between structured data pairs such as different views of an object. However, most current formulations of CFM rely on simple linear interpolants between source and target data [5, 9, 28]. While effective in practice, such interpolations may not faithfully capture the nonlinear geometry of the data manifold in latent space, potentially leading to suboptimal transitions between viewpoints.

To address this, we propose Probability Density Geodesic Flow Matching (PDG-FM), a framework that integrates data-dependent geometric regularization into conditional flow matching. Our approach builds upon Data-to-Data Flow Matching (D2D-FM), which learns deterministic flows directly between paired samples  $(x_0, x_1)$ , rather than relying on noise-to-data transitions as in conditional diffusion models. This ensures accurate data coupling and preserves structural correspondences between views.

We further refine these flows using a probability-density-based geodesic optimization, which aligns flow matching interpolants  $x_t$  with the data manifold. The local metric is defined inversely proportional to the learned data density, encouraging paths that traverse high-probability regions while penalizing off-manifold deviations. As illustrated in Fig. 1, our proposed GeodesicNet learns smooth, energy-stable interpolants that respect the underlying geometry of visual data.

Empirically, Probability Density Geodesic Flow Matching improves both perceptual quality and viewpoint consistency in novel view synthesis. Compared to diffusion and standard flow matching baselines, it produces view-consistent transformations that remain faithful to the input geometry, while retaining visual realism, even with a few inference steps. Our analysis further shows that the result-

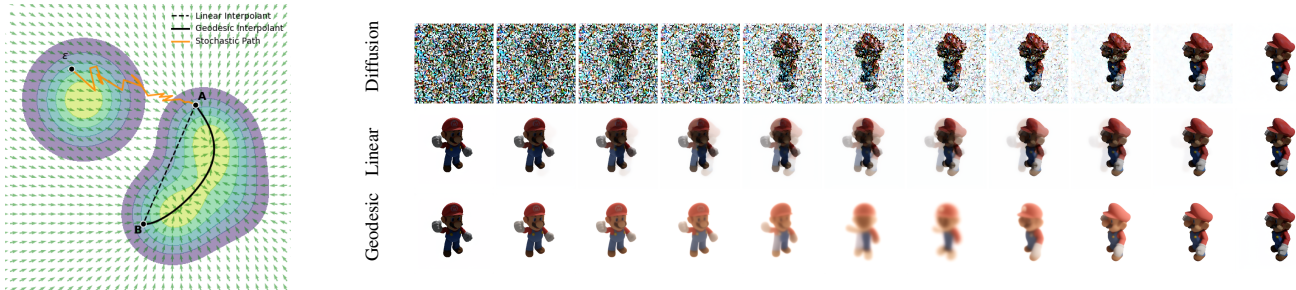


Figure 1. **From Conditional Diffusion Model to Probability Density Geodesic Flow Matching.** Conventional diffusion models learn stochastic noise-to-data transitions, often losing deterministic structure. We instead train a Data-to-Data Flow Matching network to learn continuous deterministic transformations between paired data samples  $(x_0, x_1)$ . To ensure geometric consistency, we propose to deploy a probability-density-based geodesic to aligns flow matching interpolant with high-density regions of the data manifold. This unified design couples accurate data coupling with manifold-aware regularization, yielding realistic, view-consistent transformations.

ing geodesic interpolants exhibit higher optical flow magnitude and lower Euler–Lagrange residuals, confirming their adherence to meaningful manifold structure.

Overall, our contributions are threefold:

- We propose Data-to-Data Flow Matching (D2D-FM) as a deterministic, geometry-preserving alternative to diffusion-based conditional modeling.
- We devise a data- and compute- efficient pipeline for training Probability Density Geodesic Flow Matching (PDG-FM), which leverages ambient-space distillation of density-based geodesics.
- We demonstrate that this combination achieves smoother latent transitions and improved view consistency in novel view synthesis, supported by geometric and perceptual analyses.

## 2. Related Work

### 2.1. Flow Matching in Riemannian Manifolds

Conditional Flow Matching (CFM) [1, 18, 21] provides a unified framework for learning continuous-time dynamics between distributions. It supports various conditional distributions and thus enables flexible interpolants (conditional probability paths) [10, 19]. CFM has been applied to diverse domains, including general flow matching [28] and latent bridge matching [5].

Riemannian Flow Matching (RFM) [6] extends flow matching to curved manifolds, but it assumes a fixed geometry that is independent of the data distribution, limited in modeling data-dependent conditional paths. Recent efforts have introduced data-dependent metrics through metric learning [14] or density-based formulations [32, 37], where the local metric is inversely related to the underlying probability density [4, 11]. Our work operationalizes a density-based metric within conditional flow matching, enabling data-dependent geodesic regularization directly applicable to multi-view generative modeling.

### 2.2. Novel View Synthesis with Generative Model

The emergence of large-scale 2D generative diffusion models has led to impressive progress in generating realistic objects and scenes [24, 26]. Several works [23, 25] attempt to distill priors from text-to-image diffusion models for 3D generation. However, such text-to-3D paradigms face challenges due to the semantic ambiguity of text and the computational expense of iterative optimization.

More recent efforts focus on diffusion models trained directly on multi-view posed image datasets. Zero-1-to-3 [20] first demonstrated view synthesis from paired 2D views rendered from large-scale 3D datasets [7, 8]. Yet, its outputs often suffer from limited geometric consistency across viewpoints. Subsequent works [16, 17, 36, 38] improved view consistency through architectural design and conditioning strategies, but they do not explicitly model the geometric relationships underlying cross-view consistency. In this work, we address this gap by introducing a probability-density-based geodesic formulation that regularizes latent transitions along data-adaptive paths. Through leveraging the underlying probability landscape to define geometry-consistent interpolations within the generative process, our formulation improves structural coherence and cross-view consistency.

## 3. Background

### 3.1. Conditional Flow Matching

Given a coupling distribution  $p_{0,1}$  of source and target data with marginals  $p_0$  and  $p_1$ , we can sample data pair  $(x_0, x_1) \sim p_{0,1}$ , and specify a stochastic interpolant  $x_t \sim p(x_t|t, x_0, x_1)$  at each timestep  $t \in [0, 1]$ . The conditional path must satisfy the boundary conditions that  $p(\cdot|t=0, x_0, x_1) = p_0$  and  $p(\cdot|t=1, x_0, x_1) = p_1$ .

Let  $u_t(x_t|x_0, x_1)$  denote the conditional velocity field that realizes the time-dependent marginal  $p(x_t|t, x_0, x_1)$ ,

such that their equivalence is characterized by the continuity equation under standard regularity assumptions [18, 21]. A neural vector field  $v_\theta(x_t, t)$  is trained to approximate  $u_t$  by minimizing the conditional flow matching loss:

$$\ell^{\text{CFM}}(\theta) = \mathbb{E}_{x_0, x_1, t} [\|v_\theta(x_t, t) - u_t(x_t|x_0, x_1)\|^2 |x_t]. \quad (1)$$

### 3.2. Geodesic along Data-driven Manifold

**Geodesic measurements** A geodesic defines the shortest path between two points on a Riemannian manifold, under a constant-speed parameterization. Such paths can be obtained by minimizing the length functional of a curve using the calculus of variations [2, 3].

We adopt a probability-density-based geodesic [32, 37], where the local metric tensor is defined inversely proportional to the data density. The length of a path  $\gamma : [0, 1] \rightarrow \mathbb{R}^d$  is given by:

$$S[\gamma] = \int_0^1 L(t, \gamma(t), \dot{\gamma}(t)) dt, \quad (2)$$

where  $L$  is the Lagrangian given by

$$L(t, \gamma, \dot{\gamma}) = \|\dot{\gamma}\|_{G(\gamma)}, \quad (3)$$

with the norm  $\|x\|_M = \sqrt{x^\top M x}$  scaled by a metric tensor  $G(x) = p(x)^{-2}I$  inversely proportional to the density function  $p : \mathbb{R}^d \rightarrow \mathbb{R}_+$ .

**Functional derivative** The Euler–Lagrange equation that characterizes the shortest path (geodesic) for (2) is:

$$\ddot{\gamma} + \|\dot{\gamma}\|^2 \left( I - \widehat{\gamma}\widehat{\gamma}^\top \right) \nabla \log p(\gamma) = 0, \quad (4)$$

with  $\widehat{\gamma} = \dot{\gamma}/\|\dot{\gamma}\|$  the unit velocity. This second-order ODE describes the optimal path given initial conditions (position and velocity). By calculus of variation, the functional derivative  $\frac{\delta S}{\delta \gamma}$  [37] can be derived for a constant speed parameterization as:

$$\frac{\delta S}{\delta \gamma} = \frac{-1}{p(\gamma)\|\dot{\gamma}\|} \left( \left( I - \widehat{\gamma}\widehat{\gamma}^\top \right) \nabla \log p(\gamma) + \frac{\ddot{\gamma}}{\|\dot{\gamma}\|^2} \right), \quad (5)$$

which will be leveraged in Alg. 1 for training the Geodesic Network  $\phi_\eta$ .

## 4. Methodology

Our approach, Probability Density Geodesic Flow Matching (PDG-FM), comprises two main components: (1) Data-to-Data Flow Matching (D2D-FM), a deterministic framework for mapping between paired samples in structured domains such as multi-view image synthesis; and (2) Variational Distillation of Geodesics, a geometry-regularized extension that aligns these flows with the data manifold using probability density geodesics derived from a pretrained diffusion score function. An overview of the complete framework is illustrated in Figure 2.

### 4.1. Data-to-Data Flow Matching

Conventional Flow Matching learns continuous-time dynamics from a Gaussian prior to data. In contrast, our Data-to-Data Flow Matching (D2D-FM) formulation directly learns a deterministic flow between structured data pairs  $(x_0, x_1)$ , where  $x_0$  and  $x_1$  are encoded views of the same scene under different camera poses. This formulation removes the need for a noise prior and explicitly enforces structural correspondence between paired views.

**Network Architecture** Our velocity net  $v_\theta(x_t, t, q, c)$  adopts a U-Net [27] backbone similar to that of Zero-1-to-3. Each training sample is specified by source-target camera poses  $(Q_0, Q_1)$  and their corresponding images  $(I_0, I_1)$ . The model takes as input the intermediate state  $x_t$  and time  $t$ , and is conditioned on:

- $\text{PluckerRayEmbedder}(Q_0, Q_1)$ : Target camera ray is embedded using Plücker coordinates  $r_{uv} = \psi(o, d_{uv}) = (o \times d_{uv}, d_{uv}) \in \mathbb{R}^6$  [29, 36], where  $o$  denotes the origin and  $d_{uv}$  denotes the ray direction derived from camera intrinsics  $K$  and extrinsics  $(R, T)$ . The source view serves as the canonical reference, and target rays are expressed relative to the source camera coordinate frame.
- $\mathcal{E}_{\text{clip}}(I_0)$ : CLIP-encoded semantic conditioning from the source view, which is concatenated with the relative pose between  $(Q_0, Q_1)$  and injected through cross-attention layers to guide appearance and content alignment.
- $\mathcal{E}_{\text{img}}(I_0)$ : VAE-encoded latent from source view, which is concatenated with the interpolated latent  $x_t$  as the U-Net input to preserve spatial structure.

**Training Objective** We firstly adapt the linear interpolants. The conditional path and its corresponding target velocity field are defined as:

$$x_t = (1-t)x_0 + tx_1 + \sigma_{\min}\varepsilon, \quad \varepsilon \sim \mathcal{N}(0, I), \quad (6)$$

$$u_t(x_t|x_0, x_1) = x_1 - x_0, \quad (7)$$

with a minimal variance  $\sigma_{\min} = 0.01$  to smooth the data samples. In line with [13, 28], we augment the source latent  $x_0$  according to the cosine schedule.

The velocity network  $v_\theta$  is trained to regress the time derivative of the linear interpolant:

$$\mathcal{L}_{\text{CFM}}(\theta) = \mathbb{E}_{x_0, x_1, t} [\|v_\theta(x_t, t, q, c) - (x_1 - x_0)\|^2] \quad (8)$$

### 4.2. Variational Distillation of Geodesics

To obtain flow paths aligned with the underlying data manifold geometry, we introduce GeodesicNet, a neural module that optimizes probability-density-based geodesics using a pretrained diffusion score function as a proxy for data density.

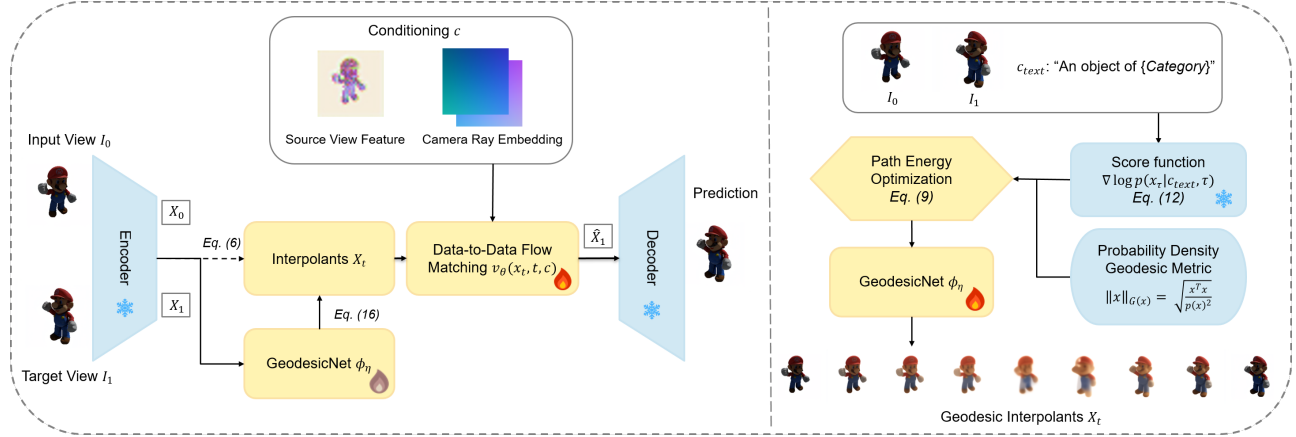


Figure 2. **Overview of the Probability Density Geodesic Flow Matching (PDG-FM) framework.** (a) *Data-to-Data Flow Matching* learns deterministic mappings between paired samples  $(x_0, x_1)$  by encoding source and target views into latent space and predicting intermediate states  $x_t$  through either linear interpolants (Eq. 6) or geodesic interpolants (Eq. 17) predicted by the GeodesicNet  $\phi_\eta$ . The velocity field  $v_\theta(x_t, t, c)$  is conditioned on source view features and Plücker ray embeddings, and its decoded outputs yield novel views consistent with the target pose. (b) *Variational Distillation of Geodesics* trains GeodesicNet  $\phi_\eta$  to produce manifold-aligned interpolants by minimizing path energy defined under the probability density geodesic metric  $\|x\|_{\mathcal{G}(x)} = \sqrt{x^\top x / p(x)^2}$ , where the density  $p(x)$  is estimated using a pretrained diffusion score function (Eq. 12). (c) The unified PDG-FM integrates both components, resulting in geometry-aware and manifold-consistent transformations for view-consistent novel view synthesis.

---

### Algorithm 1: GeodesicNet Distillation

---

**Input:** source-target Image pairs  $(I_{0,k}, I_{1,k})_{k \in \mathcal{K}}$ ;  
text prompts  $(T_k)_{k \in \mathcal{K}}$ ; DDIM timestep  $\tau$ ;  
pretrained diffusion scaling  $\beta$ ; VAE encoder  
 $\mathcal{E}_{\text{img}}$ ; CLIP encoder  $\mathcal{E}_{\text{clip}}$ .

**Output:** GeodesicNets  $\phi_\xi, \phi_\eta$ .

```

1 forall  $k \in \mathcal{K}$  do
2    $\{c_0, c_1\} \leftarrow$ 
    $\{\text{TextInversion}(\mathcal{E}_{\text{clip}}(T_k), I_{i,k})\}_{i=\{0,1\}}$ 
3    $\{x_0, x_1\} \leftarrow \{\mathcal{E}_{\text{img}}(I_i)\}_{i=\{0,1\}}$ 
4    $\{z_0, z_1\} \leftarrow \{\text{DDIM-F}(x_i, c_i, \tau)\}_{i=\{0,1\}}$ 
5    $\mathcal{T} \leftarrow \text{TimeSampler}(i)$ 
6   forall  $t \in \mathcal{T}$  do
7      $z_t \leftarrow (1-t)z_0 + tz_1 + \phi_\xi(z_0, z_1, t)$ 
8      $c_t \leftarrow (1-t)c_0 + tc_1$ 
9      $s_t \leftarrow \text{Score}(z_t, c_t, \tau, \beta)$  // Eq. (12)
10     $g_t \leftarrow \text{FuncDeriv}(z_t, v_t, a_t, s_t)$  // Eq. (5)
11     $\ell_t^\tau(\xi) \leftarrow \text{StopGrad}(g) \cdot z_t$ 
12     $\ell^\tau(\xi) = \mathbb{E}_t[\ell_t^\tau(\xi)]$ 
13    Update  $\xi$  using  $\nabla_\xi \ell^\tau(\xi)$ 
14    forall  $t \in \mathcal{T}$  do
15       $x_t \leftarrow (1-t)x_0 + tx_1 + \phi_\eta(x_0, x_1, t)$ 
16       $\ell_t^0(\eta) \leftarrow \|x_t - \text{DDIM-B}(z_t, c_t, \tau)\|^2$ 
17       $\ell^0(\eta) = \mathbb{E}_t[\ell_t^0(\eta)]$ 
18      Update  $\eta$  using  $\nabla_\eta \ell^0(\eta)$ 

```

---

**Geodesic Interpolants** We parameterize the probability density geodesic as

$$x_t = (1-t)x_0 + tx_1 + \phi_\eta(x_0, x_1, t), \quad (9)$$

with an ambient-space correction network  $\phi_\eta$  satisfying the boundary constraints  $\phi_\eta(x_0, x_1, 0) = \phi_\eta(x_0, x_1, 1) = 0$ . The network  $\phi_\eta$  is distilled from a companion teacher network  $\phi_\xi$  of the same structure but imposed in the latent space resulting from forward DDIM (DDIM-F) [30]. This dual-network architecture separates the geometric optimization (teacher) from the efficient path generation (student), enabling robust manifold-aware interpolation.

**Variational Distillation** We adopt a teacher-student distillation scheme for probability density geodesic optimization. The teacher network  $\phi_\xi$  can be updated in accordance with the shortest-path principle (2).

Given the denoising diffusion network  $\zeta$  [26], we define the DDIM-F operator [30], written  $\text{DDIM-F}(x, c, \tau)$  with initial state  $x$ , condition variable  $c$  and timestep  $\tau$ , via the first-order ODE:

$$x_0 = x; \quad \forall 0 < t < \tau: \quad (10)$$

$$\frac{d}{dt} \left( \frac{x_t}{\sqrt{\alpha_t}} \right) = \frac{d}{dt} \left( \sqrt{\frac{1 - \bar{\alpha}_t}{\alpha_t}} \right) \zeta(x_t, c, t). \quad (11)$$

The solution  $x_\tau = \text{DDIM-F}(x, c, \tau)$ , often seen as a “smoothed” version of  $x$  (denoted by  $z$  in Alg. 1), has a Stein score that can be approximated via classifier-free guidance:

$$\nabla \log p(x_\tau | c, \tau) \approx \beta \omega(\tau) (\zeta(x_\tau, c, \tau) - \zeta(x_\tau, c_{\text{neg}}, \tau)). \quad (12)$$

---

**Algorithm 2:** Geodesic Flow Matching

---

**Input:** source-target image pairs  $(I_{0,k}, I_{1,k})_{k \in \mathcal{K}}$ ;  
source-target pose pairs  $(Q_{0,k}, Q_{1,k})_{k \in \mathcal{K}}$ ;  
VAE encoder  $\mathcal{E}_{\text{img}}$ ; CLIP encoder  $\mathcal{E}_{\text{clip}}$ ;  
GeodesicNet  $\phi_\eta$ .

**Output:** VelocityNet  $v_\theta$ .

```
1 for  $k \in \mathcal{K}$  do
2    $q_k \leftarrow \text{PluckerRayEmbedder}(Q_{0,k}, Q_{1,k})$ 
3    $c_k \leftarrow \mathcal{E}_{\text{clip}}(I_{0,k})$ 
4    $\{x_{0,k}, x_{1,k}\} \leftarrow \{\mathcal{E}_{\text{img}}(I_{i,k})\}_{i=\{0,1\}}$ 
5 while training do
6   Sample  $x_0, x_1, q, c, t$ 
7    $x_t \leftarrow (1-t)x_0 + tx_1 + \phi_\eta(x_0, x_1, t)$ 
8    $v_{\text{target}} \leftarrow x_1 - x_0 + \nabla_t \phi_\eta(x_0, x_1, t)$ 
9    $\ell^v(\theta) \leftarrow \mathbb{E}[\|v_\theta(x_t, t, q, c) - v_{\text{target}}\|^2]$ 
10  Update  $\theta$  using  $\nabla_\theta \ell^v(\theta)$ 
```

---

Here  $c_{\text{neg}}$  is a negative prompt embedding that specifies unwanted, out-of-distribution instructions for the diffusion model. Our choice of hyperparameters in experiments is  $\beta = 1$ ,  $\tau = 0.6$ , and  $w(\tau) = -(1 - \bar{\alpha}_\tau)^{-1/2}$  a weighting function. We choose non-zero timestep  $\tau = 0.6$  because score functions are poorly estimated in low-density regions [31]. By operating at moderate noise levels, we populate sparse regions of the latent space, providing more reliable gradient estimates for geodesic optimization.

This enables us to perform gradient descent update using the (rescaled) functional derivative in (5):

$$z_t = (1-t)z_0 + tz_1 + \phi_\xi(z_0, z_1, t), \quad (13)$$

$$g_t = \left( I - \hat{\gamma}_t \hat{\gamma}_t^\top \right) \nabla \log p(z_t | c_t, \tau) + \frac{\tilde{\gamma}_t}{\|\hat{\gamma}_t\|^2}, \quad (14)$$

$$\ell^\tau(\xi) = \mathbb{E}_t[\text{StopGrad}(g_t) \cdot z_t] \rightarrow \min. \quad (15)$$

The alignment between teacher network  $\phi_\xi$  and student network  $\phi_\eta$  can be achieved via minimizing an MSE loss involving the backward DDIM (DDIM-B) operator:

$$x_t = (1-t)x_0 + tx_1 + \phi_\eta(x_0, x_1, t), \quad (16)$$

$$\ell^0(\eta) = \mathbb{E}_t[\|x_t - \text{DDIM-B}(z_t, c, \tau)\|^2] \rightarrow \min. \quad (17)$$

More details on variational distillation are given in Alg. 1.

### 4.3. Geodesic Flow Matching for NVS

Once the GeodesicNet  $\phi_\eta$  is ready, we apply conditional flow matching [6, 21] for training the VelocityNet  $v_\theta(x_t, t, c)$ ; see Alg. 2. VelocityNet applies the same architecture of Section 4.1. The target velocity  $v_{\text{target}}$  involves computation of time derivative of the network  $\phi_\eta$ , which can be done via forward mode of auto-differentiation (e.g. `jac_fwd` in Pytorch).

In contrast to metric flow matching (MFM) [14], we adopt a two-phase approach here, that is, (1) Learn the geodesic path parameterized with an ambient-space corrector  $\phi_\eta$ ; (2) The conditional flow matching fits  $v_\theta$  to the  $\phi_\eta$  guided paths. Such design choice is more favorable in terms of: (1) It requires relatively less data and compute to train  $\phi_\eta$ ; (2) Training and deployment of flow model  $v_\theta$  is now detached from the score-dependent Riemannian metric, and hence much more efficient.

## 5. Experiment

### 5.1. Data-to-Data Flow Matching for NVS

**Datasets** We evaluate our models on single-view novel view synthesis (NVS) using the Objaverse dataset [7], which contains over 772,870 3D objects with multi-view renderings. Following Zero-1-to-3 [20], we render 12 random views per object on a white background. For out-of-distribution (OOD) evaluation, we additionally use the Google Scanned Objects (GSO) dataset [8]. All models are trained on Objaverse and evaluated on both Objaverse test-split and GSO30 chosen by SyncDreamer [22].

**Experimental Setup** We first evaluate the effectiveness of the proposed Data-to-Data Flow Matching (D2D-FM) formulation against conventional Noise-to-Data Flow Matching and diffusion-based NVS baselines. This experiment tests whether deterministic data-pair coupling improves view consistency and reduces artifacts in novel view generation. We compare the D2D-FM with Linear Interpolants (Eq. 6) against Zero-1-to-3 [20], EscherNet [16], and Free3D [38], as well as a Noise-to-Data FM variant implemented on the same backbone.

We report quantitative results using PSNR, SSIM [35], LPIPS, CLIP Similarity (CLIP-S), and Fréchet Inception Distance (FID) [12]. Higher PSNR, SSIM, and CLIP-S indicate better image fidelity and semantic consistency, while lower LPIPS and FID denote improved perceptual realism.

**Implementation Details** All models follow the Zero-1-to-3 architecture built upon the Stable Diffusion [26], where text conditioning is replaced with source-view and pose conditioning. The CLIP [CLS] embedding and relative camera pose are linearly projected and integrated into U-Net cross-attention layers, while the VAE latents of the source and intermediate states are concatenated at the input level to preserve spatial correspondence. We employ Plücker ray embeddings through Ray Conditional Normalization (RCN) [38], enabling the model to adapt to per-pixel camera orientations. Models are trained under the same optimization settings (AdamW optimizer, batch size 256, learning rate  $1 \times 10^{-5}$ ,  $256 \times 256$  resolution) and equal training steps for a fair comparison across baselines. We report

Method	Objaverse					GSO30				
	FID ↓	CLIP-S ↑	SSIM ↑	PSNR ↑	LPIPS ↓	FID ↓	CLIP-S ↑	SSIM ↑	PSNR ↑	LPIPS ↓
Zero-1-to-3	5.9959	88.6625	0.8446	19.5850	0.0962	12.5796	90.9683	0.8536	19.3038	0.0638
Zero-1-to-3-XL	7.2006	87.1176	0.7916	17.1722	0.1505	15.7340	89.0756	0.8280	18.6022	0.0910
EscherNet	7.9058	87.9020	0.8363	18.7560	0.1061	14.7044	90.1891	0.8595	<b>20.1754</b>	0.0689
Free3D	5.5434	88.9575	0.8537	20.3222	0.0873	<b>12.0620</b>	<b>91.1424</b>	0.8581	19.5610	0.0666
Naive FM	5.5093	88.8786	0.8622	20.8246	0.0809	15.2763	89.8226	0.8631	19.7273	0.0641
Data-to-Data FM	<b>5.4324</b>	<b>88.9855</b>	<b>0.8634</b>	<b>20.8447</b>	<b>0.0809</b>	15.0543	89.5713	<b>0.8647</b>	19.8742	<b>0.0641</b>

Table 1. **Novel view synthesis performance on Objaverse and GSO datasets.** We evaluate across multiple datasets. Data-to-Data Flow Matching surpasses Noise-to-Data Flow Matching and the conditional diffusion baselines.

results using released checkpoints of Zero-1-to-3, Zero-1-to-3-XL, and EscherNet, and re-train Free3D and NaiveFM using identical training protocols as our method.

**Results** Table 1 summarizes quantitative results on Objaverse and GSO with 100 NFE(Number of Function Evaluations). Data-to-Data FM consistently outperforms Noise-to-Data FM and diffusion-based baselines in both fidelity and perceptual quality. Improvements are especially notable in FID and LPIPS, suggesting sharper detail and reduced artifacts.

Figure 3 illustrates representative results on Objaverse, showing that D2D-FM preserves structural integrity and viewpoint alignment more effectively than diffusion-based baselines. On the GSO30 dataset, our model achieves higher fidelity in novel view synthesis compared to Free3D, particularly under large viewpoint changes. As shown in Fig. 4, our generated views maintain better alignment with target poses and exhibit fewer artifacts, highlighting the advantage of learning deterministic flows directly between structured view pairs.

This advantage is more clearly demonstrated in an accelerated inference setting. Table 2 shows a fast inference comparison with only 10 NFE. Here, the Data-to-data FM outperforms the Naive FM baseline and Conditional Diffusion baseline. These findings suggest that the data-to-data framework is a more stable and efficient formulation for the conditional NVS task, providing a solid foundation for our further geodesic interpolants design.

## 5.2. Geodesic Data-to-Data Flow Matching

**Experimental Setup** We conduct experiments on the LVIS-annotated Objaverse subset to assess the effect of incorporating probability density-based geodesic interpolants into the Data-to-Data Flow Matching (FM) framework. We employ a pretrained text-to-image Stable Diffusion model [26] for both the VAE encoder-decoder and the score function proxy for the underlying data density.

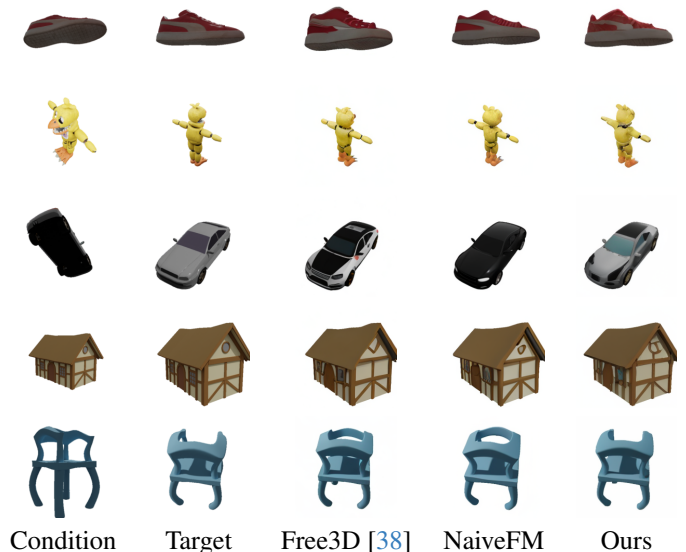


Figure 3. **Qualitative comparisons** on Objaverse. Comparison of Data-to-Data FM (with linear interpolant), the Noise-to-Data FM (Naive FM) baseline and the diffusion-based Free3D model.

Method	Objaverse			
	FID ↓	CLIP-S ↑	SSIM ↑	LPIPS ↓
Free3D	22.4533	77.9569	0.4470	0.4372
Free3D (cfg= 1)	8.9367	84.4197	0.7894	0.1493
Naive FM	5.7768	88.9998	0.8679	0.0779
Data-to-data FM	5.8223	88.9749	0.8688	0.0782

Table 2. **Novel view synthesis performance with 10 NFE.** Data-to-Data FM preserve superior performance with few inference steps.

**Implementation Details** Following Algorithm 1, we train a pair of networks,  $\phi_\xi$  and  $\phi_\eta$  jointly. The network  $\phi_\xi$  predicts geodesic interpolants  $z_t$  in the diffusion latent space by minimizing the Euler-Lagrange residual 5,

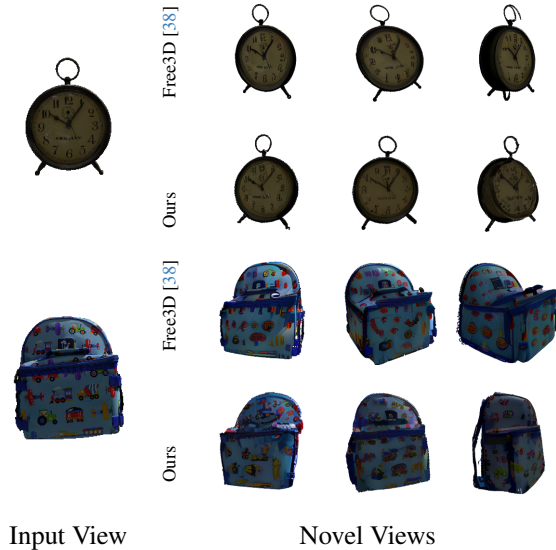


Figure 4. **Qualitative comparisons** on GSO30. Comparison of Free3D and our method (“Ours”) given the same input view.

while  $\phi_\eta$  maps these latent trajectories to the corresponding VAE space  $x_t$  and their time derivatives  $v_t$ . Condition embeddings are obtained via text inversion of CLIP-encoded prompts of the form “an object of category”, ensuring consistent conditioning across all object views.

Once the GeodesicNet  $\phi_\eta$  is obtained, we train a Data-to-Data Flow Matching model with this learned geodesic interpolants (i.e. **Geodesic FM**) using Algorithm 2. And we compare it with a variant **Linear FM**, where interpolants are computed via linear latent interpolation. Both models are fine-tuned from the pretrained velocity network used in the previous Data-to-Data Flow Matching experiment.

**Results** Table 3 reports the quantitative results comparing Geodesic FM with its linear counterpart. Incorporating geodesic interpolants yields consistent improvements in CLIP similarity, SSIM, and PSNR, demonstrating enhanced perceptual quality and geometric coherence in novel view generation. These gains suggest that accounting for the curvature of the underlying probability density guides the flow model toward more semantically consistent and physically plausible trajectories.

Moreover, the improved consistency can be traced to the interpolation geometry analyzed in Section 5.3, where geodesic paths were shown to exhibit higher optical flow magnitude and lower Euler-Lagrange residuals than linear interpolants. Together, these findings indicate that the learned probability density geodesics provide an effective prior for regularizing data-to-data transformations in flow matching, leading to novel views that remain faithful to input geometry while maintaining visual realism.

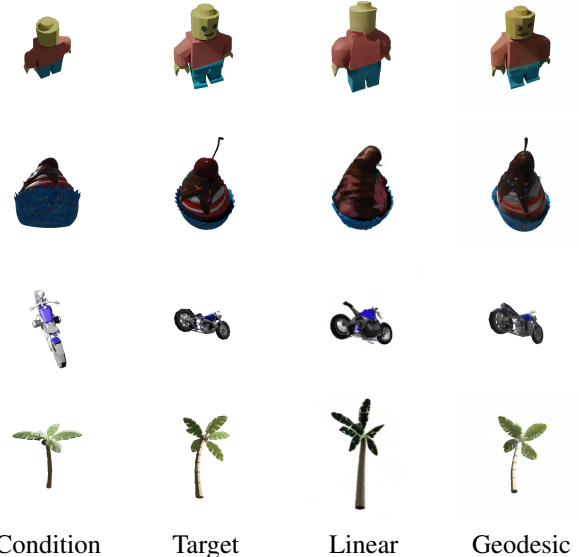


Figure 5. **Qualitative comparisons** between Geodesic FM and Linear FM on Objaverse. Visual results showing that Geodesic FM generates more geometrically faithful novel views. The improvement reflects the effect of energy-guided optimization along data-dependent geodesics.

Method	Objaverse			
	FID ↓	CLIP-S ↑	SSIM ↑	LPIPS ↓
Linear FM	11.8124	94.3476	0.8736	0.0809
Geodesic FM	10.4010	92.3368	0.8768	0.0804

Table 3. **Novel view synthesis performance with Geodesic Interpolants and Linear Interpolants.**

### 5.3. Probability Density Geodesic

We study the behavior of the proposed probability-density-based geodesic interpolants using the training procedure described in Algorithm 1. The analysis focuses on both the geometric and energetic properties of the learned paths across the GSO30 dataset.

**Interpolation Path Geometry** Perceptual Path Length (PPL) [15] is often used to measure interpolation smoothness. However, a low PPL may correspond to simple 2D cross-fading without 3D consistency. We posit that a dynamic viewpoint change implies a geometrically better path. To quantify this, we compute the Average Optical Flow Magnitude (AOFM) across 11 interpolated frames using a pretrained RAFT model [34]. A higher AOFM indicates coherent motion consistent with camera rotation rather than static blending.

Table 4 reports quantitative results, showing that



Figure 6. **Geodesic Interpolants vs Linear Interpolants.** Geodesic interpolants traverse semantically meaningful regions of the data manifold, producing perceptually consistent interpolants. In contrast, linear interpolants merely blend the two endpoints, resulting in limited structural continuity and unrealistic transitions.

geodesic interpolants achieve significantly higher AOFM compared to linear interpolants. As further visualized in Figure 6, geodesic interpolants traverse semantically meaningful image latents on the data manifold, and therefore producing perceptually consistent novel views. Whereas linear interpolants merely blend two endpoints with limited structural continuity.

Method	Setting	PPL ↓	AOFM ↑
Linear	6 objs	0.2130	1.0411
Initial	6 objs	0.5710	6.4773
Geodesic	6 objs	0.5023	13.6968

Table 4. **Geodesic Path Study Results.** We measure PPL, and AOFM for linear, DDIM-initialized, and geodesic interpolants across the dataset.

**Analysis of Path Energy** We further analyze the geodesic gradient norm, and it is defined as the magnitude of the functional derivative in Eq. 5. A lower norm signifies better satisfaction of the Euler-Lagrange condition and thus closer adherence to the high-density regions.

As shown in Figure 7, the geodesic interpolants maintains lower energy residuals across time compared to both their pre-optimization counterparts and linear interpolants. This behavior aligns with their higher optical flow magnitude and perceptual coherence, confirming that the energy-guided optimization (Alg. 1) effectively regularizes the interpolation trajectory.

## 6. Conclusion

We presented a prototype framework for studying latent-space structure in generative models via geodesic-informed

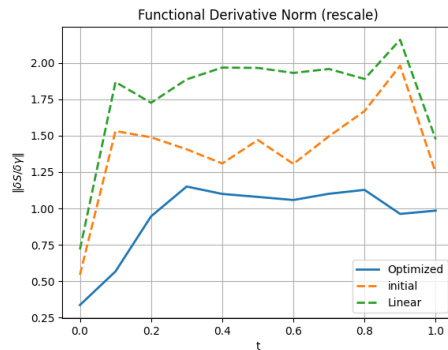


Figure 7. **Comparison of Geodesic Gradient Norm across Time** for geodesic interpolants, their pre-optimization counterparts, and linear interpolants on training dataset. The optimized geodesic paths have lower residuals thus indicating better satisfaction of the Euler-Lagrange condition, aligning with improved perceptual and geometric consistency.

flow matching. By leveraging a pretrained score function as a proxy for data density, our method allows the exploration of meaningful paths in the latent space, demonstrated on a viewpoint transformation task. Experiments show that geodesic-informed interpolation can capture semantic structure more faithfully than naïve linear flows, highlighting the potential of latent-space geometry for guiding generative processes.

We note that the current approach involves multiple training stages and is computationally intensive, which limits its scalability. Nevertheless, it offers a concrete and extensible framework for examining the interplay between latent geometry and generative dynamics, paving the way toward more efficient formulations of geodesic-informed generative modeling.

## References

- [1] Michael Samuel Albergo and Eric Vanden-Eijnden. Building normalizing flows with stochastic interpolants. In *The Eleventh International Conference on Learning Representations*, 2023. 1, 2
- [2] Georgios Arvanitidis, Lars Kai Hansen, and Søren Hauberg. Latent space oddity: on the curvature of deep generative models, 2021. 3
- [3] Georgios Arvanitidis, Miguel González-Duque, Alison Poupin, Dimitrios Kalatzis, and Soren Hauberg. Pulling back information geometry. In *Proceedings of The 25th International Conference on Artificial Intelligence and Statistics*, pages 4872–4894. PMLR, 2022. 3
- [4] Olivier Bousquet, Olivier Chapelle, and Matthias Hein. Measure based regularization. In *Advances in Neural Information Processing Systems*. MIT Press, 2003. 2
- [5] Clément Chadebec, Onur Tasar, Sanjeev Sreetharan, and Benjamin Aubin. Lbm: Latent bridge matching for fast image-to-image translation, 2025. 1, 2
- [6] Ricky T. Q. Chen and Yaron Lipman. Flow matching on general geometries, 2024. 2, 5
- [7] Matt Deitke, Dustin Schwenk, Jordi Salvador, Luca Weihs, Oscar Michel, Eli VanderBilt, Ludwig Schmidt, Kiana Ehsani, Aniruddha Kembhavi, and Ali Farhadi. Objaverse: A universe of annotated 3d objects. In *Proceedings of the IEEE/CVF conference on computer vision and pattern recognition*, pages 13142–13153, 2023. 2, 5
- [8] Laura Downs, Anthony Francis, Nate Koenig, Brandon Kinman, Ryan Hickman, Krista Reymann, Thomas B McHugh, and Vincent Vanhoucke. Google scanned objects: A high-quality dataset of 3d scanned household items. In *2022 International Conference on Robotics and Automation (ICRA)*, pages 2553–2560. IEEE, 2022. 2, 5
- [9] Tobias Fischer, Samuel Rota Bulò, Yung-Hsu Yang, Nikhil Keetha, Lorenzo Porzi, Norman Müller, Katja Schwarz, Jonathon Luiten, Marc Pollefeys, and Peter Kotschieder. Flowr: Flowing from sparse to dense 3d reconstructions. In *Proceedings of the IEEE/CVF International Conference on Computer Vision*, pages 27702–27712, 2025. 1
- [10] Anne Gagneux, Ségolène Martin, Rémi Emonet, Quentin Bertrand, and Mathurin Massias. A visual dive into conditional flow matching. In *ICLR Blogposts 2025*, 2025. <https://dl.heeere.com/conditional-flow-matching/blog/conditional-flow-matching/>. 2
- [11] Pablo Groisman, Matthieu Jonckheere, and Facundo Sapienza. Nonhomogeneous Euclidean first-passage percolation and distance learning. *Bernoulli*, 28(1):255–276, 2022. 2
- [12] Martin Heusel, Hubert Ramsauer, Thomas Unterthiner, Bernhard Nessler, and Sepp Hochreiter. Gans trained by a two time-scale update rule converge to a local nash equilibrium. *Advances in neural information processing systems*, 30, 2017. 5
- [13] Jonathan Ho, Chitwan Saharia, William Chan, David J Fleet, Mohammad Norouzi, and Tim Salimans. Cascaded diffusion models for high fidelity image generation. *Journal of Machine Learning Research*, 23(47):1–33, 2022. 3
- [14] Kacper Kapusniak, Peter Potaptchik, Teodora Reu, Leo Zhang, Alexander Tong, Michael Bronstein, Joey Bose, and Francesco Di Giovanni. Metric flow matching for smooth interpolations on the data manifold. *Advances in Neural Information Processing Systems*, 37:135011–135042, 2024. 2, 5
- [15] Tero Karras, Samuli Laine, and Timo Aila. A style-based generator architecture for generative adversarial networks. In *Proceedings of the IEEE/CVF conference on computer vision and pattern recognition*, pages 4401–4410, 2019. 7
- [16] Xin Kong, Shikun Liu, Xiaoyang Lyu, Marwan Taher, Xiaojuan Qi, and Andrew J Davison. Eschnet: A generative model for scalable view synthesis. In *Proceedings of the IEEE/CVF Conference on Computer Vision and Pattern Recognition*, pages 9503–9513, 2024. 2, 5
- [17] Lingen Li, Zhaoyang Zhang, Yaowei Li, Jiale Xu, Wenbo Hu, Xiaoyu Li, Weihao Cheng, Jinwei Gu, Tianfan Xue, and Ying Shan. Nvcomposer: Boosting generative novel view synthesis with multiple sparse and unposed images. In *Proceedings of the Computer Vision and Pattern Recognition Conference*, pages 777–787, 2025. 2
- [18] Yaron Lipman, Ricky T. Q. Chen, Heli Ben-Hamu, Maximilian Nickel, and Matthew Le. Flow matching for generative modeling. In *The Eleventh International Conference on Learning Representations*, 2023. 1, 2, 3
- [19] Yaron Lipman, Marton Havasi, Peter Holderrieth, Neta Shaul, Matt Le, Brian Karrer, Ricky T. Q. Chen, David Lopez-Paz, Heli Ben-Hamu, and Itai Gat. Flow matching guide and code, 2024. 2
- [20] Ruoshi Liu, Rundi Wu, Basile Van Hoorick, Pavel Tokmakov, Sergey Zakharov, and Carl Vondrick. Zero-1-to-3: Zero-shot one image to 3d object. In *Proceedings of the IEEE/CVF international conference on computer vision*, pages 9298–9309, 2023. 2, 5
- [21] Xingchao Liu, Chengyue Gong, and qiang liu. Flow straight and fast: Learning to generate and transfer data with rectified flow. In *The Eleventh International Conference on Learning Representations*, 2023. 1, 2, 3, 5
- [22] Yuan Liu, Cheng Lin, Zijiao Zeng, Xiaoxiao Long, Lingjie Liu, Taku Komura, and Wenping Wang. Syncdreamer: Generating multiview-consistent images from a single-view image, 2024. 5
- [23] Luke Melas-Kyriazi, Iro Laina, Christian Rupprecht, and Andrea Vedaldi. Realfusion: 360deg reconstruction of any object from a single image. In *Proceedings of the IEEE/CVF conference on computer vision and pattern recognition*, pages 8446–8455, 2023. 2
- [24] Dustin Podell, Zion English, Kyle Lacey, Andreas Blattmann, Tim Dockhorn, Jonas Müller, Joe Penna, and Robin Rombach. Sdxl: Improving latent diffusion models for high-resolution image synthesis. *arXiv preprint arXiv:2307.01952*, 2023. 2
- [25] Ben Poole, Ajay Jain, Jonathan T. Barron, and Ben Mildenhall. Dreamfusion: Text-to-3d using 2d diffusion, 2022. 1, 2
- [26] Robin Rombach, Andreas Blattmann, Dominik Lorenz, Patrick Esser, and Björn Ommer. High-resolution image

- synthesis with latent diffusion models. In *Proceedings of the IEEE/CVF conference on computer vision and pattern recognition*, pages 10684–10695, 2022. 2, 4, 5, 6
- [27] Olaf Ronneberger, Philipp Fischer, and Thomas Brox. U-net: Convolutional networks for biomedical image segmentation. In *International Conference on Medical image computing and computer-assisted intervention*, pages 234–241. Springer, 2015. 3
- [28] Johannes Schusterbauer, Ming Gui, Pingchuan Ma, Nick Stracke, Stefan Andreas Baumann, Vincent Tao Hu, and Björn Ommer. *FMBoost: Boosting Latent Diffusion with Flow Matching*, pages 338–355. Springer Nature Switzerland, 2024. 1, 2, 3
- [29] Vincent Sitzmann, Semon Rezhchikov, Bill Freeman, Josh Tenenbaum, and Fredo Durand. Light field networks: Neural scene representations with single-evaluation rendering. *Advances in Neural Information Processing Systems*, 34: 19313–19325, 2021. 3
- [30] Jiaming Song, Chenlin Meng, and Stefano Ermon. Denoising diffusion implicit models. In *ICLR*, 2021. 4
- [31] Yang Song and Stefano Ermon. Generative modeling by estimating gradients of the data distribution. *Advances in neural information processing systems*, 32, 2019. 5
- [32] Peter Sorrenson, Daniel Behrend-Urriarte, Christoph Schnörr, and Ullrich Köthe. Learning distances from data with normalizing flows and score matching, 2025. 2, 3
- [33] Junshu Tang, Tengfei Wang, Bo Zhang, Ting Zhang, Ran Yi, Lizhuang Ma, and Dong Chen. Make-it-3d: High-fidelity 3d creation from a single image with diffusion prior. In *Proceedings of the IEEE/CVF international conference on computer vision*, pages 22819–22829, 2023. 1
- [34] Zachary Teed and Jia Deng. Raft: Recurrent all-pairs field transforms for optical flow. In *European conference on computer vision*, pages 402–419. Springer, 2020. 7
- [35] Zhou Wang, A. C. Bovik, H. R. Sheikh, and E. P. Simoncelli. Image quality assessment: from error visibility to structural similarity. *Trans. Img. Proc.*, 13(4):600–612, 2004. 5
- [36] Yifeng Xiong, Haoyu Ma, Shanlin Sun, Kun Han, Hao Tang, and Xiaohui Xie. Light field diffusion for single-view novel view synthesis. *IEEE Access*, 2025. 2, 3
- [37] Qingtao Yu, Jaskirat Singh, Zhaoyuan Yang, Peter Henry Tu, Jing Zhang, Hongdong Li, Richard Hartley, and Dylan Campbell. Probability density geodesics in image diffusion latent space. In *Proceedings of the Computer Vision and Pattern Recognition Conference*, pages 27989–27998, 2025. 2, 3
- [38] Chuanxia Zheng and Andrea Vedaldi. Free3d: Consistent novel view synthesis without 3d representation. In *Proceedings of the IEEE/CVF Conference on Computer Vision and Pattern Recognition*, pages 9720–9731, 2024. 2, 5, 6, 7

# GeodesicNVS: Probability Density Geodesic Flow Matching for Novel View Synthesis

## Supplementary Material

### 7. Derivations

This section provides detailed derivations of the Euler–Lagrange equation and functional derivative for the density-based geodesic formulation.

We recall the weighted length functional

$$S[\gamma] = \int_0^1 L(t, \gamma(t), \dot{\gamma}(t)) dt, \quad \gamma : [0, 1] \rightarrow \mathbb{R}^d \quad (18)$$

with the Lagrangian written in three equivalent forms:

$$L(t, \gamma, \dot{\gamma}) = \|\dot{\gamma}\|_{G(\gamma)} \quad (19)$$

$$= p(\gamma)^{-1} \|\dot{\gamma}\| \quad (20)$$

$$= \sqrt{\dot{\gamma}^\top G(\gamma) \dot{\gamma}}, \quad (21)$$

where the metric tensor is defined as

$$G(\gamma) = p(\gamma)^{-2} I. \quad (22)$$

#### 7.1. Euler-Lagrange Equation

The Euler-Lagrange equation is given by:

$$\frac{d}{dt} \left( \frac{\partial L}{\partial \dot{\gamma}} \right) - \frac{\partial L}{\partial \gamma} = 0. \quad (23)$$

Compute partial derivatives using  $L = p(\gamma)^{-1} \|\dot{\gamma}\|$ :

$$\frac{\partial L}{\partial \dot{\gamma}} = p(\gamma)^{-1} \hat{\gamma}, \quad (24)$$

$$\frac{\partial L}{\partial \gamma} = -p(\gamma)^{-1} \nabla \log p(\gamma) \|\dot{\gamma}\|. \quad (25)$$

The time derivative yields:

$$\begin{aligned} \frac{d}{dt} \left( \frac{\partial L}{\partial \dot{\gamma}} \right) &= -p(\gamma)^{-1} (\nabla \log p(\gamma) \cdot \dot{\gamma}) \hat{\gamma} \\ &\quad + p(\gamma)^{-1} \frac{(I - \hat{\gamma} \hat{\gamma}^\top) \ddot{\gamma}}{\|\dot{\gamma}\|}. \end{aligned} \quad (26)$$

Substituting into Euler–Lagrange:

$$\begin{aligned} -p(\gamma)^{-1} (\nabla \log p(\gamma) \cdot \dot{\gamma}) \hat{\gamma} + p(\gamma)^{-1} \frac{(I - \hat{\gamma} \hat{\gamma}^\top) \ddot{\gamma}}{\|\dot{\gamma}\|} \\ + p(\gamma)^{-1} \nabla \log p(\gamma) \|\dot{\gamma}\| = 0. \end{aligned} \quad (27)$$

Multiply by  $p(\gamma)$  and simplify using  $\hat{\gamma} = \frac{\dot{\gamma}}{\|\dot{\gamma}\|}$ :

$$\frac{(I - \hat{\gamma} \hat{\gamma}^\top) \ddot{\gamma}}{\|\dot{\gamma}\|} - (\nabla \log p(\gamma) \cdot \dot{\gamma}) \hat{\gamma} + \nabla \log p(\gamma) \|\dot{\gamma}\| = 0. \quad (28)$$

Note the identity:

$$\nabla \log p(\gamma) \|\dot{\gamma}\| - (\nabla \log p(\gamma) \cdot \dot{\gamma}) \hat{\gamma} = \|\dot{\gamma}\| (I - \hat{\gamma} \hat{\gamma}^\top) \nabla \log p(\gamma). \quad (29)$$

Thus:

$$\frac{(I - \hat{\gamma} \hat{\gamma}^\top) \ddot{\gamma}}{\|\dot{\gamma}\|} + \|\dot{\gamma}\| (I - \hat{\gamma} \hat{\gamma}^\top) \nabla \log p(\gamma) = 0. \quad (30)$$

Multiplying by  $\|\dot{\gamma}\|$  and using the fact that for constant-speed paths,  $(I - \hat{\gamma} \hat{\gamma}^\top) \ddot{\gamma} = \ddot{\gamma}$ , recovers the equivalent formulas in the main text (4):

$$\boxed{\ddot{\gamma} + \|\dot{\gamma}\|^2 (I - \hat{\gamma} \hat{\gamma}^\top) \nabla \log p(\gamma) = 0.} \quad (31)$$

#### 7.2. Functional Derivative

The functional derivative is:

$$\frac{\delta S}{\delta \gamma} = \frac{\partial L}{\partial \gamma} - \frac{d}{dt} \left( \frac{\partial L}{\partial \dot{\gamma}} \right). \quad (32)$$

Using our previous results:

$$\begin{aligned} \frac{\delta S}{\delta \gamma} &= -p(\gamma)^{-1} \nabla \log p(\gamma) \|\dot{\gamma}\| + p(\gamma)^{-1} (\nabla \log p(\gamma) \cdot \dot{\gamma}) \hat{\gamma} \\ &\quad - p(\gamma)^{-1} \frac{(I - \hat{\gamma} \hat{\gamma}^\top) \ddot{\gamma}}{\|\dot{\gamma}\|}. \end{aligned} \quad (33)$$

Factor out the projection identity  $(I - \hat{\gamma} \hat{\gamma}^\top)$ :

$$\frac{\delta S}{\delta \gamma} = -\frac{1}{p(\gamma) \|\dot{\gamma}\|} [(I - \hat{\gamma} \hat{\gamma}^\top) (\nabla \log p(\gamma) \|\dot{\gamma}\|^2 + \ddot{\gamma})]. \quad (34)$$

For constant-speed paths,  $(I - \hat{\gamma} \hat{\gamma}^\top) \ddot{\gamma} = \ddot{\gamma}$ , yielding:

$$\boxed{\frac{\delta S}{\delta \gamma} = \frac{-1}{p(\gamma) \|\dot{\gamma}\|} \left[ (I - \hat{\gamma} \hat{\gamma}^\top) \nabla \log p(\gamma) + \frac{\ddot{\gamma}}{\|\dot{\gamma}\|^2} \right].} \quad (35)$$

This represents the normal component of the path variation, as noted in the main text (5), consistent with the geometric decomposition in the Euler–Lagrange equation.

### 7.3. Probability density along the path

To compute the functional derivative norm, we estimate the probability density along paths. Following [1, 3], we compute relative probabilities  $p(\gamma(t))/p(\gamma(a))$  since absolute density estimation is challenging.

For the conservative vector field  $\nabla \log p$ , the relative log-probability between  $\gamma(a)$  and  $\gamma(t)$  is path-independent:

$$\log \tilde{p}_a(\gamma(b)) := \log p(\gamma(b)) - \log p(\gamma(a)) \quad (36)$$

$$= \int_a^b \dot{\gamma}(t)^\top \nabla \log p(\gamma(t)) dt. \quad (37)$$

We approximate this integral using the trapezoidal rule. Let  $f(\tau) = \dot{\gamma}(\tau)^\top \nabla \log p(\gamma(\tau))$  and sample the path at  $n+1$  equally spaced points  $t_i = a + i/n$  for  $i = 0, \dots, n$ . The relative log-probability at  $\gamma(t_i)$  is:

$$\log \tilde{p}_a(\gamma(t_i)) \approx \frac{1}{n} \left( \frac{f(a)}{2} + \sum_{k=1}^{i-1} f(t_k) + \frac{f(t_i)}{2} \right). \quad (38)$$

This enables computation of  $\tilde{p}_a(\gamma(t_i)) = p(\gamma(t_i))/p(\gamma(a))$  along the curve, which is used in evaluating (5) for comparison of geodesic gradient norm in Fig. 7.

## 8. Further Implementation Details

This section provides comprehensive implementation details for the key components of our Probability Density Geodesic Flow Matching (PDG-FM) framework, complementing the methodological descriptions in Sec. 4.

### 8.1. Data-to-Data Flow Matching Implementation

**Training Configuration** Our Data-to-Data Flow Matching (D2D-FM) models, including Free3D, Naive FM, and our proposed variants, are trained using the linear interpolant formulation from Eq. 6. All models inherit the publicly released checkpoint from Zero-1-to-3 [20] to ensure fair comparison.

Training is conducted in the latent space at  $32 \times 32$  resolution, obtained by encoding  $256 \times 256$  input images through the VAE from Stable Diffusion [26], which provides an  $8\times$  downscaling factor. We train all models for 20,000 steps with a global batch size of 256, using the AdamW optimizer with learning rate  $1 \times 10^{-5}$  and standard weight decay.

### 8.2. Variational Distillation of Geodesics

The geodesic distillation follows Algorithm 1 using the LVIS-annotated Objaverse subset with 12 random views per object and category annotations.

**Preprocessing Pipeline** Image pairs at  $512 \times 512$  resolution are encoded to  $64 \times 64$  ambient latents  $x_0, x_1$  using the VAE encoder. For each object pair with shared category text prompt, we apply Text Inversion [2] to fine-tune CLIP text embeddings, yielding dedicated embeddings  $c_0, c_1$  for respective views. The inversion runs for 500 steps with learning rate 0.005 using AdamW optimizer.

The ambient latents  $x_0, x_1$  and their corresponding text embeddings  $c_0, c_1$  are then processed through DDIM-F( $x, c, \tau$ ) with  $\tau = 0.6$ , classifier-free guidance scale  $\text{cfg} = 1$ , and 30 NFE (using a 50-step DDIM scheduler) to obtain the final latent pairs  $z_0, z_1$  in the DDIM-F latent space.

**GeodesicNet Optimization** The teacher network  $\phi_\xi$  operates in the DDIM-F latent space and is optimized using AdamW with learning rate  $1 \times 10^{-6}$  and uniform timestep sampling. The optimization uses score gradients computed via Eq. 12, with conditioning employing  $c_t - c_{\text{neg}}$  where  $c_t = (1-t)c_0 + tc_1$  represents time-linear text conditioning. The negative prompt targets unrealistic image artifacts: "A doubling image, unrealistic, artifacts, distortions, unnatural blending, ghosting effects, overlapping edges, harsh transitions, motion blur, poor resolution, low detail".

The student network  $\phi_\eta$  operates in ambient latent space and is optimized using AdamW with learning rate  $1 \times 10^{-3}$ , minimizing the MSE loss between predicted  $x_t$  and DDIM-B( $z_t, c_t, \tau$ ) reconstructions. Both networks use identical UNet architectures with 128 channels and 2 residual blocks.

### 8.3. Probability Density Geodesic Flow Matching

We train two D2D-FM variants: Linear FM using linear interpolants and Geodesic FM using geodesic interpolants from the trained GeodesicNet  $\phi_\eta$ . Both models initialize from the Zero-1-to-3 checkpoint and train at  $64 \times 64$  latent space for 40,000 steps with global batch size 32.

### 8.4. Computational Efficiency

All models are trained on NVIDIA RTX A6000 GPUs with 48GB memory.

Our two-phase approach (geodesic distillation followed by flow matching) provides significant efficiency advantages: GeodesicNet training requires fewer samples than end-to-end metric flow matching; flow model training is detached from score function evaluation, avoiding expensive density gradient computations during FM training; and the modular design enables independent improvements to geodesic estimation and flow matching components.

## 9. Further Experiment Results

**CFM Ablation** We analyze two key design choices in Data-to-Data Flow Matching: noise augmentation and training timestep sampling. Tab. 5 presents the quantitative evaluation.

For noise augmentation, we compare our default setting (eps=400) with a lower-noise variant (eps=50). Both configurations are evaluated using 100 inference steps. Results demonstrate that moderate noise augmentation (eps=400) consistently outperforms the low-noise alternative across all metrics, indicating that appropriate noise regularization prevents overfitting while preserving semantic consistency.

For timestep sampling, we compare our default lognormal sampling (std=1, mean=0) against discrete uniform sampling strategies optimized for few-step inference. The discrete distributions  $U_{10}$  and  $U_4$  sample training timesteps that align with specific inference steps (10 and 4 NFE respectively). Our default lognormal sampling is evaluated using 10 inference steps. Notably, these discrete strategies outperform continuous uniform sampling when evaluated at their target inference steps, with  $U_{10}$  achieving the best overall balance across evaluation metrics.

Method	Objaverse				
	FID ↓	CLIP-S ↑	SSIM ↑	PSNR ↑	LPIPS ↓
D2D-FM	5.4324	88.9855	0.8634	20.8447	0.0809
D2D-FM(eps=50)	5.8050	88.3582	0.8532	20.0291	0.0883
D2D-FM	5.8223	88.9749	0.8688	21.3045	0.0782
D2D-FM, $U_{10}$	5.5146	88.9185	0.8706	21.5952	0.0737
D2D-FM, $U_4$	7.4414	88.1954	0.8784	22.2092	0.0743

Table 5. Ablation study of noise augmentation (top) and timestep sampling (bottom) in D2D-FM.

**Extended D2D-FM Qualitative Results** Figures 9 and 10 provide additional qualitative comparisons of our Data-to-Data FM against Noise-to-Data FM and Free3D baselines. Our method maintains superior structural consistency and detail preservation, particularly in the challenging 10 NFE setting. For Free3D, we use cfg=1 at 10NFE as conditional diffusion models exhibit significant performance degradation with classifier-free guidance during accelerated inference. The deterministic coupling in D2D-FM enables more faithful geometry reconstruction and reduces artifacts observed in diffusion-based approaches under limited inference budgets.

**Extended PDG-FM Qualitative Results** Fig. 8 presents additional comparisons between our Probability Density Geodesic FM and linear interpolation baselines. Visual analysis shows that our geodesic Data-to-Data FM (PDG-FM) preserves finer details across viewpoint changes,

as geodesic interpolants maintain manifold consistency throughout transformations. These observations align with our quantitative findings in the main text, demonstrating the benefits of manifold-aware interpolation.



Figure 8. Extended Qualitative Results of Geodesic FM and Linear FM on Objaverse.

## References

- [1] Chen-Hao Chao, Wei-Fang Sun, Bo-Wun Cheng, and Chun-Yi Lee. On investigating the conservative property of score-based generative models. In *International Conference on Machine Learning*, pages 4076–4095. PMLR, 2023. 2
- [2] Rinon Gal, Yuval Alaluf, Yuval Atzmon, Or Patashnik, Amit Haim Bermano, Gal Chechik, and Daniel Cohen-or. An image is worth one word: Personalizing text-to-image generation using textual inversion. In *The Eleventh International Conference on Learning Representations*. 2
- [3] Qingtao Yu, Jaskirat Singh, Zhaoyuan Yang, Peter Henry Tu, Jing Zhang, Hongdong Li, Richard Hartley, and Dylan Campbell. Probability density geodesics in image diffusion latent space. In *Proceedings of the Computer Vision and Pattern Recognition Conference*, pages 27989–27998, 2025. 2, 3

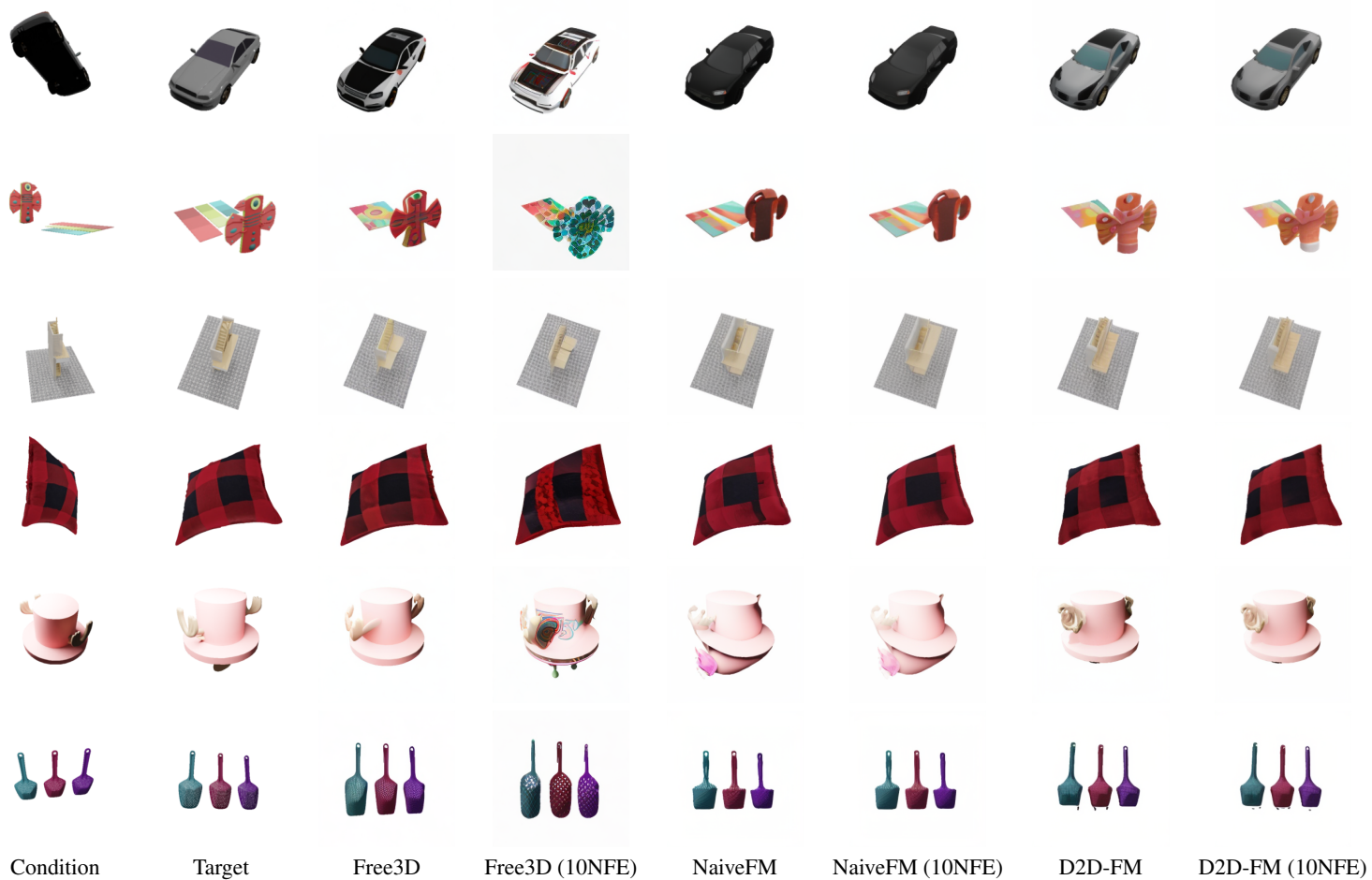


Figure 9. **Extended Qualitative Results** on Objaverse.

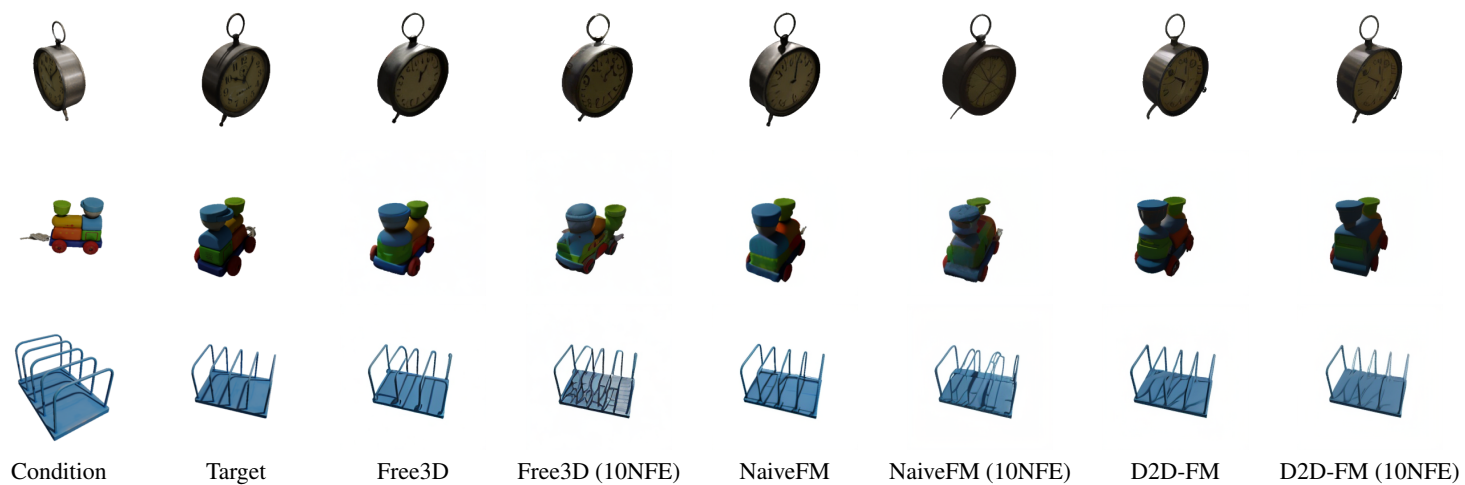


Figure 10. **Extended Qualitative Results** on GSO30.